A New Flowing Afterglow-Guided Ion Beam Tandem Mass Spectrometer. Applications to the Thermochemistry of Polyiodide Ions

Khanh Do, Timothy P. Klein, Cynthia Ann Pommerening, and Lee S. Sunderlin

Department of Chemistry, Northern Illinois University, DeKalb, Illinois, USA

A new flowing afterglow-guided ion beam tandem mass spectrometer has been constructed. The tandem mass spectrometer has a linear quadrupole–octopole–quadrupole geometry. The apparatus has been successfully tested for the measurement of reaction rates and endothermic reaction thresholds. The new instrument has been used to determine 0 K bond strengths in two polyiodide ions: $D(I_2–I^-)$ = 126 ± 6 kJ/mol and $D(I_2–I_3^-)$ = 49 ± 6 kJ/mol. These values compare well to recent computational results. Electron affinity $(EA)(I_3)$ = 4.15 ± 0.12 eV can be derived from this work and values in the literature. (J Am Soc Mass Spectrom 1997, 8, 688–696) © 1997 American Society for Mass Spectrometry

In the 1960s, Ferguson and co-workers invented the flowing afterglow device for the study of ion–molecule reaction chemistry [1]. The flowing afterglow is a fast flow reactor in which ions created at the upstream end of a flow tube are swept down the tube by the buffer gas [2]. The ions react with neutral molecules added downstream, and the ionic reaction products are monitored by using a mass spectrometer. The basic flowing afterglow technology has been elaborated in many ways in recent years [2].

Tandem mass spectrometry has a longer history, dating back to the work of Thompson in 1910 [3]. One use of tandem mass spectrometry is to study collision-induced dissociation (CID). CID, now the most widely practiced type of tandem mass spectrometry [4], involves subjecting the mass-analyzed output of one mass spectrometer to a collision, and then analyzing the products in another mass spectrometer. The first experiments of this type were performed on a magnetic sector instrument [5]. Later experiments used two quadrupole mass spectrometers with a collision gas cell in between [6, 7]. A substantial improvement was initiated by Yost and Enke, who used an rf-only quadrupole ion guide in the collision region in order to minimize product scattering [8]. The central rf-only quadrupole had been previously used for photodissociation [9] and metastable decomposition [10] studies. The use of a more efficient octopole ion guide [11] instead of a quadrupole ion guide was also pioneered in this period [12].

Thus, both the flowing afterglow and the tandem mass spectrometer have been developed substantially in the last thirty years. More recently, instruments that combine the two techniques have been developed. The early tandem mass spectrometer of Teloy and Gerlich [12] utilized a labyrinthine ion source operating at 0.01 torr to thermalize ions before mass analysis. A flowing afterglow-triple quadrupole was first demonstrated in 1985 [13, 14]. In a development from the other direction, a flowing afterglow ion source was added [15] onto a guided ion beam tandem mass spectrometer of magnet–octopole–quadrupole geometry [16]. Other groups have also built related instruments [11, 17]. The reasons are straightforward: the flowing afterglow is an extremely versatile ion source for tandem mass spectrometry, and the tandem mass spectrometer is a useful detector for the flowing afterglow.

We have constructed a novel instrument that consists of a flowing afterglow combined with a tandem mass spectrometer of quadrupole–octopole–quadrupole geometry. In the first part of this article, the design and testing of the new instrument are detailed. In the second part, applications of the new instrument are demonstrated through an investigation of the chemistry of polyiodide anions.

Polyhalide anions have been the subject of extensive investigation [18]. However, most of these studies involve x-ray diffraction studies of geometries or solution-phase studies of complexation equilibria. While the equilibrium constants can be used to derive bond enthalpies in solution, these bond strengths are greatly dependent on solvent effects. Very little reliable information is available on the gas-phase bond strengths [19]. However, as a model for main-group bonding motifs, the gas-phase ions are more relevant than the solvated ions. Also, the bare polyhalide ions are a challenging test case for computational chemists, as

Address reprint requests to Lee Sunderlin, Department of Chemistry, Northern Illinois University, DeKalb, IL 60115.

1044-0305/97/$17.00
PII S1044-0305(97)00116-5

Received November 20, 1996
Revised February 17, 1997
Accepted February 17, 1997

discussed below. I_3^- is a model as well for studies of photodissociation dynamics [20].

Polyhalide ions, particularly polyiodides, are also of practical significance. Formation of the dark iodine-starch complex upon addition of iodine/iodide is still used as a test for the presence of starch; this complex involves the I_5^- anion [21]. Polyhalide anions also have significance as analytical tools for the detection of halide ions [22] because of their characteristic UV-visible spectra. Such species have also been used as dopants to modify the electronic properties of polymers [23].

There have been several attempts to measure or estimate the bond strength in I_3^-. The first, by Hogness and Harkness [24], was also the first to discuss the chemistry of negative ions in a mass spectrometer. They concluded that $D(I^-–I_2) > D(I–I) = 149$ kJ/mol [25], although these results assumed a mechanism that is apparently incorrect.

Later, two estimates of the thermochemistry of I_3^- were made. Both used the empirical Kapustinskii relation [26], which involves correlating the bond strengths in ionic solids to the ionic radii of the cation and anion. Topol [27] derived $D(I^-–I_2) = 100$ kJ/mol from the heats of formation of the rubidium and cesium triiodides, while Finch, Gates, and Peake [28] derived $D(I^-–I_2) = 356$ kJ/mol from the heats of formation for a variety of salts. Clearly, these results are not in good agreement.

$D_e(I^-–I_2)$ was calculated by using several basis sets of quadratic configuration interaction at the single, double, and triple [QCISD(T)] level to be 126–137 kJ/mol (112–115 kJ/mol with corrections for zero-point vibrational energy and basis set superposition) [29]. More recently, Sharp and Gellene have carried out calculations on I_3^- by using both coupled cluster theory and density functional theory (DFT) [30]. They derive a bond strength of $D_e(I^-–I_2) = 114$ kJ/mol from coupled cluster theory and 128–154 kJ/mol at various levels of DFT. These values can be converted using the calculated vibrational frequencies to $D_o = 112$ kJ/mol and 126–152 kJ/mol, respectively. They also note that the DFT calculations that give the most accurate results for the I_2^- molecule, give I_3^- bond strengths at the lower end of the range cited [30]. While the linear I_3^- molecule might seem to be a simple computational subject, substantial difficulties are caused by the large number of electrons, relativistic effects, and the need for very diffuse orbitals to properly model anions [29, 30].

Sharp and Gellene also calculated $D_e(I_3^-–I_2)$ by using DFT, but the molecule was too large for adequate coupled cluster theory calculations. The results are in the range 47–77 kJ/mol. Adjusting for zero-point energies by using the calculated vibrational frequencies gives $D_o(I_3^-–I_2)$ values of 43–73 kJ/mol. Again, the levels of theory that gave the best results for I_2^- gave results in the lower end of the range. There have been no gas-phase experimental results for the bond strength of this molecule. A reliable experimental value for both bond strengths would thus be a useful benchmark for calculations on difficult anions of this nature.

Lin and Hall have also carried out Hartree–Fock calculations on I_3^- and I_5^-, as well as other polyhalide and polyhalonium ions [31]. However, they concentrate on the nature of the bonding and do not report bond strengths for these molecules.

Experimental

The design details of the new flowing afterglow tandem mass spectrometer used in these experiments are discussed below. The apparatus consists of an ion source region, a flow reactor, and a vacuum chamber containing a quadrupole mass filter, an octopole ion guide, a second quadrupole mass filter, and a detector. A schematic cross section of the instrument is shown in Figure 1.

Ion Source Region

The ion source region is located in a four-way stainless steel cross. Various ion sources are built onto flanges and attached to the cross. The ion source used in these experiments is a dc discharge that consists of a straight tungsten or nichrome wire attached to a high voltage feedthrough. The filament operates at 500–2500 V with 0.3–10 mA of emission. Another flange contains an electron impact (EI) ion source that consists of a rhenium filament spot welded between two stainless steel rods, which are attached to a vacuum feedthrough. A grounded rhenium wire mesh grid is held ca. 5 mm beyond the filament as an electron target. On the same flange is the buffer gas inlet, which is equipped with a "shower head" to disperse the buffer gas flow. Both the dc discharge and the EI flanges are mounted on side arms of the cross to eliminate direct lines of sight from the ionization sources to the detector. The ion source flanges typically have one or more inlets for reagent gases.

Flow Tube

The flow tube is a 92 cm × 7.3 cm i.d. (inner diameter) [7.62 cm o.d. (outer diameter)] stainless steel pipe with five neutral reagent inlets evenly spaced every 15 cm from the upstream end of the tube. Each inlet is typically connected to an on/off valve and then a metering valve. The upstream end of the flow tube is connected to the ion source cross. The downstream end of the flow tube is connected to a flange that is bolted to the main chamber, such that the flow tube protrudes 6.4 cm into the chamber.

A stainless steel pipe (74 cm long × 12.7 cm o.d.) encloses the flow tube except for holes corresponding to the gas inlets. The temperature of the flow tube can be changed by placing coolant, such as liquid nitrogen, into the outer pipe.

The pressure in the flow tube at the middle gas inlet is measured by a capacitance manometer referenced to the low pressure in the detector chamber. The helium flow is controlled by a mass flow controller that is

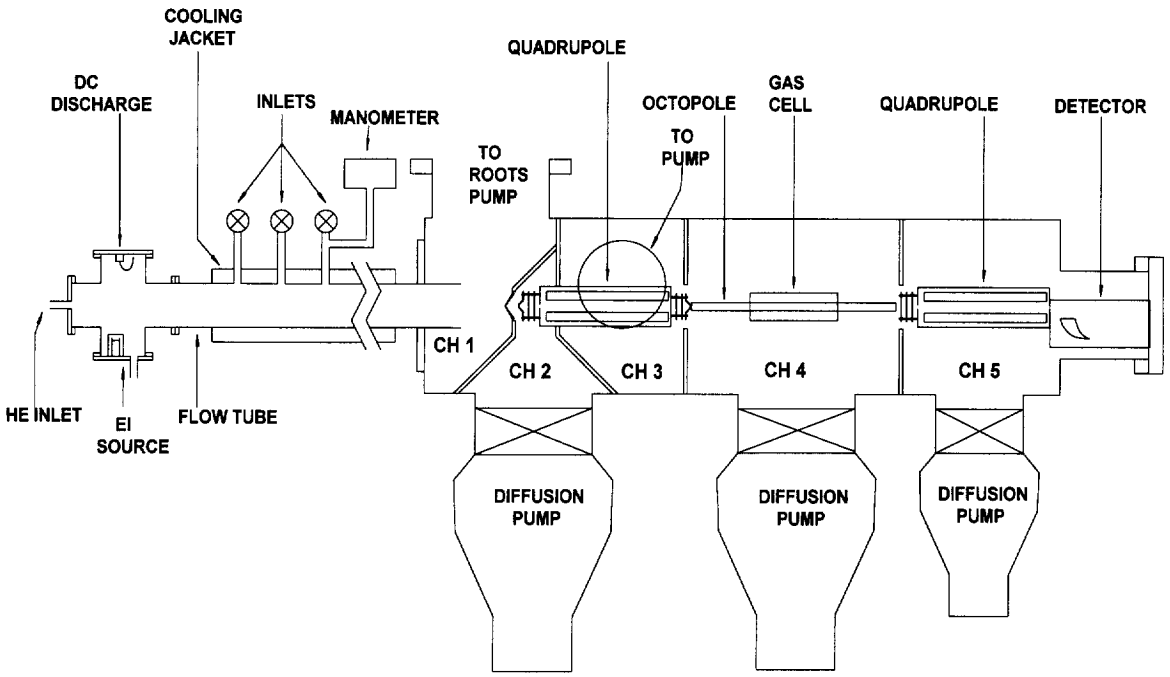

Figure 1. Schematic diagram of the flowing afterglow-tandem mass spectrometer. Chambers 1–5 are denoted by "CH."

calibrated against a wet-test meter. The helium flows through a coil of 3/8 in. o.d. stainless steel tubing 200 cm long that is filled with molecular sieves and is cooled by liquid nitrogen to remove condensible impurities. The typical pressure in the flow tube is 0.4 Torr, and the typical flow rate is 200 standard cm^3/s.

For kinetics studies, neutral reagent gas is introduced into the flow tube via a ring inlet. The ring inlet is a 5.5 cm o.d. loop of 1/8 in. stainless steel tubing with 12 holes (0.6 mm in diameter) facing upstream. This is mounted on a 130 cm long × 1/4 in. o.d. stainless steel tube extending through the ion source cross and into the flow tube through a vacuum fitting in the flange directly opposite the flow tube. The position of the ring inlet inside the flow tube is adjustable. The ring inlet is centered in the flow tube by two steel guide pins welded onto the loop.

The gas flow rate to the ring inlet is determined with the use of a glass vacuum manifold (separately pumped by a mechanical pump) of 2.078 L calibrated volume. The pressure in the glass manifold is measured by a capacitance manometer also referenced to the pressure in the detector chamber. Since $PV = nRT$ at the low pressure in the gas manifold, the gas flow rate F is calculated by using eq 1, where t = time. A Labview 3.1 (National Instruments)

$$F = \frac{dn}{dt} = \frac{d(PV/RT)}{dt} = \frac{V}{RT}\frac{dP}{dt} \quad (1)$$

program monitors the pressure as a function of time and calculates the flow rate.

The Main Chamber

The main chamber is a rectangular stainless steel box with outer dimensions of 30 cm × 30 cm × 91 cm, custom machined by GNB Corporation (Hayward, CA). It is divided into five separate regions by 0.64 cm thick stainless steel interior partitions. The first chamber is pumped by a 615 L/s roots blower backed by a 63 L/s mechanical pump. The blower is connected to the top of the front chamber by 23 cm i.d. PVC pipe, a section of flexible stainless steel bellows, and an electropneumatic gate valve with an 18 cm port. The typical operating pressure in this region is around 0.2 torr, as measured by a thermocouple gauge. The internal wall separating the front and second chamber has a 4.44 cm opening in the center. Mounted on this opening is a stainless steel plate with a 150° nose cone and a 6.3 mm aperture. This plate is electrically isolated from the chamber by a teflon ring. Covering the aperture is a molybdenum disk with a 0.5 mm orifice. Ions are gently extracted through the orifice by applying a potential (typically 0–2 V) by using a home built power supply. The disk is coated with colloidal graphite (Acheson) to prevent static charge buildup on any nonconductive materials that may condense on the disk.

Quadrupole 1

The ions are then focused through four electrostatic lenses 0.9 cm apart into the first quadrupole (Q1) (Extrel model 7-270-9). The first lens is a 139° nose cone with a 4 mm aperture. The second lens has a 13 mm aperture

and the third lens has a 4 mm aperture. These three lenses are mounted onto Q1. The fourth lens is the entrance plate of the quadrupole. These lenses and the front of Q1 reside in chamber 2 and are centered in an opening in the wall between chambers 2 and 3 by a teflon cylinder machined to fit snugly around the end of the quadrupole. The bulk of Q1 and its exit lenses reside in chamber 3. The four exit lenses are essentially identical to the entrance lenses. The quadrupole consists of 1.6 cm × 22.9 cm cylindrical rods with ceramic mounts encased in a vented stainless steel enclosure. A teflon cylinder surrounds the back of the quadrupole and the lenses. It is centered in the opening in the chamber wall between chambers 3 and 4 with an aluminum collar.

The quadrupole utilizes a 1.2 MHz oscillator and a 300 W power supply. The maximum m/z of this mass filter is 720. The voltages on the entrance and exit lenses are individually controlled by a home built resistor network, with a 150 V power supply.

Chamber 2 is pumped by a 2400 L/s oil diffusion pump backed by a 8.3 L/s mechanical pump. Chamber 3 is pumped through an elbow attached to the side of the chamber by a 1200 L/s diffusion pump backed by a 5.0 L/s mechanical pump. The baseline pressure in these chambers is 2×10^{-7} torr as measured by a pair of uncalibrated Bayard-Alpert ionization gauges. The pressure in the second chamber is typically 10^{-4} torr when the flowing afterglow is running.

Octopole and Collision Gas Reaction Cell

The ions from Q1 then enter the octopole in chamber 4. The octopole [11] provides stronger trapping in the transverse directions than the more common quadrupole ion guide. It consists of eight 35.6 cm long × 0.32 cm cylindrical stainless steel rods and a pair of ceramic mounts. The central half of the octopole is enclosed in a 17.5 cm long × 4.4 cm i.d. aluminum gas cell. This cell has two gas inlets and a socket for a miniature resistive temperature device. One inlet is connected to a capacitance manometer with digital readout. The other inlet is used to introduce the collision gas, the flow of which is controlled by a variable leak valve. Chamber 4 is pumped by a 2400 L/s diffusion pump backed by a 8.3 L/s mechanical pump.

The rf trapping voltage for the octopole is produced by a function generator and amplified by an rf power amplifier. This voltage is then isolated by a home-built resonant inductor coil circuit. The octopole typically operates at a resonance frequency of 8.2 MHz. The amplitude of the rf voltage on the octopole is typically 500 V. Tests with the charge transfer reaction of Ar^+ with O_2, where the product has ~1 eV (1 eV = 96.5 kJ/mol) of kinetic energy, indicate that 150 volts provides essentially complete trapping. The dc potential of the octopole is supplied by a ±100 V power supply.

Quadrupole 3 and Detector

From the octopole, the ions are focused into a second Extrel quadrupole (Q3), which is in chamber 5. A set of entrance lenses with 1.27 cm apertures spaced 0.9 cm apart is mounted on Q3. The lens voltages are controlled by an ionizer control module. The Q3 electronics are nearly identical to those of Q1. Chamber 5 is pumped by a 1200 L/s diffusion pump backed by a 5 L/s mechanical pump. The pressure is measured by an uncalibrated Bayard-Alpert ion gauge and is typically 3×10^{-7} torr.

Q3 is mounted on the detector as part of a flange mounted mass filter assembly. The electron multiplier operates in pulse-counting mode and is equipped with a conversion dynode. The signal is amplified and sent to a PC, where data collection and display is controlled through Labview software (National Instruments). An AT-MIO-16X board controls the quadrupole mass setting, controls the octopole dc offset, and reads the gas cell pressure.

Kinetics Calibrations

Bimolecular reaction rate coefficients k^{II} are calculated using eq 3 [32], where F_{He} and F_B are the flow rates of the helium buffer gas and the neutral reagent in s.t.p. cm^3/s, P_{He} is the flow tube pressure in torr, T is the flow tube temperature in Kelvin, z is the physical reaction distance in centimeters, and the scalar is a collection of unit conversion factors and instrumental parameters.

$$A^{\pm} + B \rightarrow \text{products} \quad (2)$$

$$k^{II} = -(d \ln [A^{\pm}]/dz) F_{He}^2 P_{He}^{-2} T^2 F_B^{-1} \times (1.10 \times 10^{-20}) \text{ cm}^3/\text{s} \quad (3)$$

In our experiments, we employ a movable ring inlet (see *Flow Tube*). The intensity of $A^{\pm}$ is monitored as the physical distance from the center of the ring inlet to the end of the flow tube is varied. Reactions 4–7 were studied to test the ability of the instrument to measure

$$N_2^+ + CO_2 \rightarrow CO_2^+ + N_2 \quad (4)$$

$$Ar^+ + H_2 \rightarrow ArH^+ + H \quad (5)$$

$$Fe(CO)_4^- + O_2 \rightarrow Fe(CO)_2O^- + CO_2 + CO \quad (6)$$

$$Ar^+ + O_2 \rightarrow O_2^+ + Ar \quad (7)$$

accurate rate coefficients. Table 1 shows the reaction rate coefficients reported in the literature and the average rate coefficients measured by this instrument for these processes. The reaction rate coefficients measured by this instrument are in good agreement with the

Table 1. Bimolecular reaction rate coefficient calibration measurements[a]

Reaction	Literature k^{II}	k^{II}, this work
4	72–90	70
5	92	91
6	1.53	1.6
7	3.9–6.2	7.5

[a]Reaction rate coefficients in units of 10^{-11} cm^3/s. Literature values from [43].

literature values, considering that the typical uncertainty in measurements by the flowing afterglow technique is ±20%. The precision determined from multiple measurements is generally ±10% or less. The results for reaction 5 are shown in Figure 2.

The end correction, ϵ, is the x intercept of the plot of ln [A^-] versus reaction distance [2, 32]. The end correction is caused primarily by a nonuniform initial distribution of the gas from the ring inlet. Applying this method with several different reactions gives an average end correction of −13 ± 27 mm. The relatively small value obtained is consistent with the uniform mixing of reagent gas at the ring inlet.

Energy-resolved CID Experiments

We likewise tested the capability of the instrument to measure translational energy thresholds for CID of thermalized ions produced in the flow tube. The CID threshold energy is determined by modeling the intensity of product ions as a function of the reactant ion kinetic energy in the lab frame, E_{lab}. The reactant ion beam energy zero is measured by using the octopole as a retarding field analyzer [11, 16]. The first derivative of the beam intensity as a function of energy is approximately Gaussian, with a full-width at half-maximum (FWHM) of 0.5–2.0 eV. E_{lab} is given by the octopole rod offset voltage measured with respect to the center of the Gaussian fit. Conversion to energy in the center-of-mass (CM) frame is accomplished by use of $E_{CM} = E_{lab}m/(m + M)$, where m and M are the masses of the neutral and ionic reactants, respectively. This energy is corrected at low offset energies to account for truncation of the ion beam as described in [16].

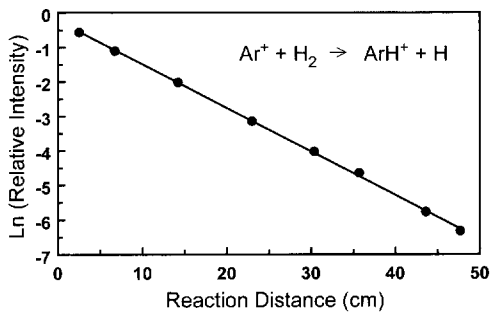

Figure 2. Ion intensity decay plot as a function of distance for the reaction between Ar^+ and H_2.

Total cross sections for reaction, σ_{total}, are calculated using eq 8 [16], where I is

$$I = I_0 \exp(-\sigma_{total} n l) \quad (8)$$

the intensity of the reactant ion beam, I_0 is the intensity of the incoming ion beam ($=I + \Sigma I_i$), I_i are the intensities for each product ion, n is the number density of the neutral collision gas, and l is the effective collision cell length. Individual product cross sections σ_i are equal to $\sigma_{total}(I_i/\Sigma I_i)$. Because the pressure of the collision gas drops toward the ends of the collision cell and is nonzero outside the nominal collision region, l is not necessarily equal to the physical length of the collision cell, but must be determined experimentally. To do this, the extent of a reaction with a known absolute total cross section was measured and then the effective collision cell length was calculated. The simple atom-transfer reaction 5, where ion mass discrimination and scattering effects are minimal, was studied for this purpose [16]. Comparison to the known energy-dependent reaction cross section over a 0.01–5 eV (CM) collision energy range gives an effective path length of 13 ± 2 cm. The physical length of the gas cell is 18 cm.

To derive CID threshold energies, the threshold region of the data is fitted to the model functions [33] given in eqs 9 and 10, where $\sigma(E)$ is the cross section for formation of the

$$\sigma(E) = \sigma_o(E - E_T)^n/E \quad (9)$$

$$\sigma(E) = \sigma_0\Sigma_i[g_i P_D(E, E_i)(E + E_i - E_T)^n/E] \quad (10)$$

product ion at center-of-mass energy E, E_T is the desired threshold energy, σ_0 is a scaling factor, P_D is the probability of an ion with a given amount of energy dissociating within the experimental window (~30 μs), and i denotes vibrational states having energy E_i and population $g_i(\Sigma g_i = 1)$. The adjustable parameter n is related to the shape of the cross section curve and is generally between 1 and 2 for CID reactions. P_D is calculated using the Rice–Ramsperger–Kassel–Marcus (RRKM) formalism. Equation 9 does not include ion lifetime and internal energy effects, while eq 10 is always used where ion lifetime or internal energy effects are significant. The CRUNCH program written by Professor Armentrout and co-workers was used in the threshold analysis described above. The systems studied to test the capability of the instrument to measure CID energy thresholds include:

$$NO_2^+(CH_3OH) \rightarrow NO_2^+ + CH_3OH \quad (11)$$

$$NO_2^+(H_2O) \rightarrow NO_2^+ + H_2O \quad (12)$$

$$NO^+(H_2O) \rightarrow NO^+ + H_2O \quad (13)$$

Table 2. Reaction threshold calibration measurements

Reaction	Literature threshold[a]	Threshold, this work[a]	Collision gas	n[b]
11	80 ± 10[c]	81 ± 15	Ar	1.6 ± 0.3
12	62 ± 10[c]	53 ± 5	Ar	1.3 ± 0.1
13	77[d]	65 ± 10	Ne	1.3 ± 0.4
14	57[d]	54 ± 5	Ar	1.3 ± 0.2
15	132[d]	118 ± 13	Ar	1.5 ± 0.3
16	95,[d] 105 ± 6[e]	108 ± 18	Ar, Ne	1.5 ± 0.5

[a]Values in kJ/mol.
[b]See text for a discussion of the fitting parameter n.
[c][44].
[d][45].
[e][15].

$$NO^+(NO) \rightarrow NO^+ + NO \quad (14)$$

$$H^+(H_2O)_2) \rightarrow H_3O^+ + H_2O \quad (15)$$

$$N_4^+ \rightarrow N_2^+ + N_2 \quad (16)$$

Table 2 compares CID energy thresholds in this work and its corresponding literature values. These reactions were chosen because their thermochemistry was reasonably well known and because they have low-frequency vibrational modes. Low frequency modes, which are more easily excited by energetic collisions with other gases, are useful to test whether the thermalized ions are reexcited during extraction from the flow tube [15]. The results in Table 2 show differences between the literature values and the present results of 8 ± 5 kJ/mol; on average, the present results are 5 kJ/mol lower than the literature values. This suggests that the instrument is both reasonably precise and reasonably accurate.

The fact that the present results are on average slightly below the literature data may be due to chance. However, three experimental factors could also responsible. A small amount of collisional reheating would explain the data; however, no reproducible effects of changing the voltages on the ion optics was observed. This suggests that the temperature of the ions is not strongly dependent on the energy with which they are extracted from the flow tube.

Another possible source of slightly low measured thresholds is contact potentials on the octopole rods, which could cause barriers to ion transmission during the retarding field analysis of the ion energy zero. The error associated with this measurement can be 0.1 eV in the lab frame [11]. Future tests of this issue will be done by using time-of-flight measurements on the ion beam [11, 16].

A final possibility is that ions are dissociated by more than one collision with the target gas. An ion that is not sufficiently energized by one collision with the target gas may gain enough energy in a second collision to be above the reaction threshold. Thus, such collisions can lead to a measured threshold that is too low. The calibration data were taken at low pressures (0.01 to 0.05 mtorr), which minimizes the chance of double collisions. It is estimated that, at most, 4% of the ions that collide with one target gas molecule then collide with a second target gas molecule. The data (and the derived reaction thresholds) were independent of the gas cell pressure over the above range within experimental resolution. The effect of secondary collisions is therefore small, although it may be a few hundredths of an electron volt.

A more rigorous procedure that accounts for multiple collisions is to linearly extrapolate data taken at several pressures to a zero pressure cross section [34]. This procedure eliminates the effects of double collisions at the cost of increased scatter. While it does not completely eliminate the effect of triple or higher order collision effects, these events are of negligible probability.

The data in these experiments are affected by two other sources of broadening. One is the thermal motion of the collision gas (Doppler broadening), and the other is the kinetic energy distribution of the reactant ion (which is approximated by a Gaussian function with the experimental FWHM). Both of these factors are accounted for by the CRUNCH program [16].

Results and Discussion

When small amounts of iodine are added to the flow tube, I^-, I_2^-, and I_3^- are the main species observed. The I^- is due to dissociative attachment of an electron to I_2, while I_2^- is due to collisionally stabilized attachment. At higher flow rates, the I^- and I_2^- are depleted, and I_3^- and I_5^- are the dominant ions. Indeed, under conditions where there are 5–10 × 10^4 counts/s of I_3^- and I_5^-, there are only roughly 5 counts/s each of I^- and I_4^- observed. The larger ions I_n^- (n = 3, 4, 5) are due to collisionally stabilized attachment of I_2 to I_{n-2}^-. The observation of I_4^- indicates that it is stable on at least a time scale of tens of microseconds, but the low intensity suggests that the ion is not very strongly bound. To optimize the intensity of I_3^- and I_5^-, iodine is dissolved in isopropanol, the solution is heated, and the resulting mixture of vapors is let into the ion source region. Other solvents are not as effective as isopropanol. Apparently, this solvent acts as both a carrier gas to drive the iodine vapor into the ion source, and as a "chaperone" [14] to promote clustering. The chaperone effect involves formation of a cluster between I^- or I_3^- and the abundant isopropanol in the flow tube, followed by displacement of the isopropanol by I_2. This is probably more efficient than stabilization by the flow tube buffer gas. A small amount of the I^--isopropanol cluster can be observed in the mass spectra at intermediate flow conditions, supporting this mechanism. Unfortunately, it is difficult to maintain the optimum source conditions for an extended length of time, and thus the reactant ion signal was not stable for more than about 15 min.

The cross sections for CID of I_3^- and I_5^- with xenon

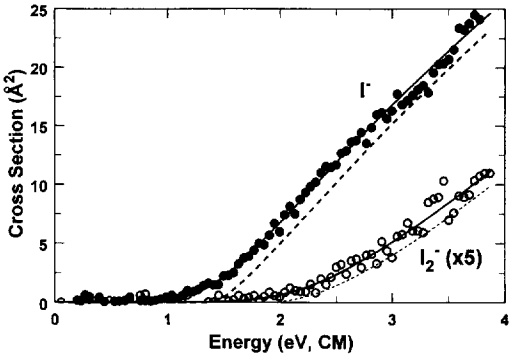

Figure 3. Appearance curves for collision-induced dissociation of I_3^- as a function of kinetic energy in the center-of-mass frame. The solid lines are the model appearance curves calculated using eq 10 and convoluted as discussed in the text. The dashed lines are the unconvoluted fits. The fitting parameters are given in Table 3.

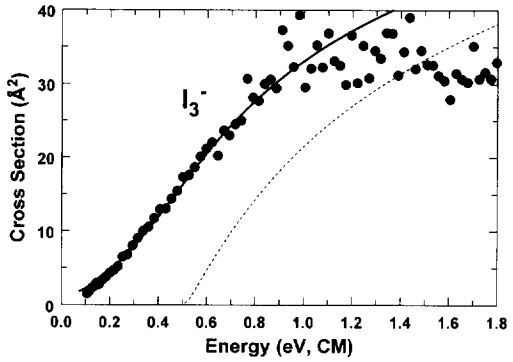

Figure 4. Appearance curve for collision-induced dissociation of I_5^- as a function of kinetic energy in the center-of-mass frame. The solid line is the model appearance curve calculated using eq 10 and convoluted as discussed in the text. The dashed line is the unconvoluted fit. The fitting parameters are given in Table 3.

are shown in Figures 3 and 4. The products observed are given in reactions 17–19. Additionally, a small amount of I^- was observed in the CID of I_5^-. The intensity of this product was insufficient for detailed study.

$$I_3^- \rightarrow I^- + I_2 \quad (17)$$

$$I_3^- \rightarrow I + I_2^- \quad (18)$$

$$I_5^- \rightarrow I_3^- + I_2 \quad (19)$$

For I_3^-, the two products seen correspond to cleavage of an I_2–I bond with a competition between I_2 and I for possession of the extra electron. The electron affinities of I and I_2 are 3.059 and 2.52 ± 0.10 eV, respectively [35]. Thus, process 18 is 0.54 ± 0.10 eV more endothermic than process 17. This is consistent with the higher threshold energy and smaller cross section for the latter process.

The data for reactions 17 and 19 were fit by using the modeling procedure outlined above. The frequencies necessary for deriving the internal energy and RRKM parameters for these reactions were taken from the calculations of Sharp and Gellene [30]. The frequencies are remarkably low, ranging from 66 to 134 cm^{-1} for I_3^-, and 12 to 157 cm^{-1} for I_5^-. Thus, the internal energies of the two molecules are 10 kJ/mol and 22 kJ/mol, respectively. The effect of ion lifetimes is negligible for I_3^-. For I_5^-, the ion lifetime effect (RRKM shift) is about 1 kJ/mol if the reaction is assumed to have a loose, productlike transition state, and about 2 kJ/mol if the reaction is assumed to have a tight, reactantlike transition state. The data reported in Table 3 are for the loose transition state, and the ±1 kJ/mol uncertainty is taken into account in the final error limit. Because the ion internal energy and the RRKM shift are taken into account, the reaction thresholds correspond to bond energies (or enthalpies) at 0 K.

Table 3. CID threshold measurements[a]

Reaction	Threshold	n
17	126 ± 6	1.5 ± 0.2
18	184 ± 14	2[b]
19	49 ± 6	1.2 ± 0.2

[a]Threshold values in kJ/mol. See text for discussion of n.
[b]n is held to 2 for reaction 18.

Because of the low intensity and the instability of the parent ion signal, extrapolation of the data to zero pressure results in very large error limits. However, analysis of data sets collected at high collision cell pressures (0.1 to 0.3 mtorr) shows lower apparent CID thresholds than the low pressure (less than 0.05 mtorr) data reported. Extrapolation of the *thresholds* as a function of pressure suggests that the thresholds reported here are too low by 2–3 kJ/mol. Because this procedure does not necessarily account for secondary collisions accurately, we choose not to include this effect in our reported results. The likely pressure effects are well within the error limits in all cases.

The fitting procedure for reaction 18 is made difficult by a competitive shift [36] caused by reaction 17. The competition between reactions 17 and 18, which is dominated by reaction 17 over the energy range studied, cannot be simply accounted for by using the modeling techniques discussed above. It is clear, however, that the cross section for reaction 18 will be more severely depleted near its threshold. Thus, the observed cross section shows a slow rise from the apparent threshold. This sort of curve is difficult to fit, particularly when the signal-to-noise level is mediocre. Therefore, it was decided to fit the data using $n = 2$, a choice that fits the data well. With this assumption regarding the cross section form, a threshold of 184 ± 14 kJ/mol was derived, where the error limit is estimated based on the extra assumptions necessary for fitting the data (the precision is ±6 kJ/mol). The difference between the thresholds for reactions 17 and 18, 0.60 ± 0.16 eV, should be the difference between the electron affinities

(EAs) of I and I_2. Since EA(I) = 3.059 eV [35], $EA(I_2)$ = 2.46 ± 0.16 eV can be derived. This is very close to the value of 2.52 ± 0.10 eV that is considered the best available [35]. Several other values for $EA(I_2)$ in the range 2.4–2.6 eV are listed in [35]; the present result is not sufficiently precise to determine which measurement is best.

The bond energies at 0 K derived in this work can be converted into bond energies at 298 K using the calculated frequencies [30]. The results are $D^{298}(I_2\text{–}I^-)$ = 123 ± 6 kJ/mol and $D^{298}(I_2\text{–}I_3^-)$ = 45 ± 6 kJ/mol. The bond enthalpies are higher by the work term (ΔPV, or RT): $DH^{298}(I_2\text{–}I^-)$ = 126 ± 6 kJ/mol and $DH^{298}(I_2\text{–}I_3^-)$ = 47 ± 6 kJ/mol. Adding the bond enthalpies to $\Delta_f H^{298}(I_{2(g)})$ = 62.3 kJ/mol [35] and $\Delta_f H^{298}(I^-_{(g)})$ = −188.2 ± 0.8 kJ/mol [35] gives $\Delta_f H^{298}(I^-_{3(g)})$ = −252 ± 6 kJ/mol and $\Delta_f H^{298}(I^-_{5(g)})$ = −237 ± 9 kJ/mol.

There have been extensive studies of polyiodide ions in solution. Measurements of the equilibrium constant for reaction 17 as a function of temperature have been used to derive $\Delta H(23)$ = 17.0 ± 0.6 kJ/mol in aqueous solution [37]. $\Delta G(23)$ in other solvents is as large as 48 kJ/mol [38]. Bond strengths in the solid state have also been measured [27], and ΔH for reaction 20 varies from 7–16 kJ/mol. The differences in bond strengths are due to solvent effects,

$$MI_{3(s)} \rightarrow MI_{(s)} + I_{2(s)} \qquad (20)$$

and bond strengths in the gas phase and in solution can be used to derive the enthalpy of solvation of I_3^-. The enthalpies of solvation of I^- and I_2 are 291 kJ/mol [39] and 41 kJ/mol [40], respectively. The sum of these two numbers is 332 kJ/mol. Subtracting the difference between the gas-phase and solution bond strengths gives $\Delta_{sol}H^{298}(I_3^-)$ = −223 ± 6 kJ/mol. This is slightly less than that for I^-, which is consistent with generally weaker solvation of larger anions [41].

From this work and previously known thermochemistry, it is possible to use eq 21 to derive the EA of I_3. Several indirect determinations of $D_e(I_2\text{–}I)$ have been

$$EA(I_3) = EA(I) + D(I_2\text{–}I^-) - D(I_2\text{–}I) \qquad (21)$$

recently discussed and averaged [42] to give 23 kJ/mol. This leads to $D_o(I_2\text{–}I)$ = 21 ± 10 kJ/mol, where the zero-point energy is taken from the I_3^- frequencies [30] and the error limits are a conservative estimate. This can be combined with $D_o(I_2\text{–}I^-)$ = 126 ± 6 kJ/mol and EA(I) = 3.059 eV to give $EA(I_3)$ = 4.15 ± 0.12 eV. The bond strength in neutral I_5 has not been determined, but the EA of I_5 is probably even higher than that of I_3.

The bond strengths derived here can be compared to previous determinations. For I_3^-, there are several values in the literature, which are summarized in Table 4. The original mass spectrometric conclusions [24] were interpreted in a manner now known to be outmoded. One of the empirical results based on the heat of formation of triiodide salts is impressively accurate [27] while another [28] is clearly unreasonable. Both sets of ab initio calculations give bond strengths that are 11–14 kJ/mol below the experimental result, while density functional theory gives bond strengths that are 0–26 kJ/mol high. The DFT bond strengths for I_5^- range from 2 kJ/mol below to 28 kJ/mol above the experimental value. Given the difficulties of studying polyiodide anions using computational techniques, this level of agreement is promising.

Table 4. Measurements of $D(I^-\text{–}I_2)$

Technique	Bond strength (kJ/mol)	Reference
Reaction exothermicity bracketing	>149	24
Estimate	100	27
Estimate	356	28
QCISD(T)[a]	126–137[b]	29
	112–115[c]	
CCSD(T)[d]	112	30
DFT[e]	126–152	
CID	126 ± 6	This work

[a]Calculated using the QCISD(T) method.
[b]Uncorrected for zero-point energy (ZPE) and basis set superposition error (BSSE).
[c]Corrected for ZPE and BSSE.
[d]Calculated using the CCSD(T) method.
[e]Calculated using density functional theory.

Acknowledgments

The authors thank the American Society for Mass Spectrometry for partial support of this work through a research award to L.S.S. Acknowledgment is also made to the Donors of The Petroleum Research Fund, administered by the American Chemical Society, for the partial support of this research. We thank Amoco and Deepcoat Inc., for donations of equipment; Professor Peter Armentrout, Professor Robert Squires, Professor Kent Ervin, and Professor Morley Russell for useful advice; and Charles Caldwell, Larry Gregersen, Dan Edwards, and Phillip Stone for assistance with the construction of the instrument. We also thank Professor Greg Gellene for preliminary communication of his results.

References

1. Fehsenfeld, F. C.; Schmeltekopf, A. L.; Goldan, P. D.; Schiff, H. I.; Ferguson, E. E. *J. Chem. Phys.* **1966,** *44,* 4087–4094.
2. Graul, S. T.; Squires, R. R. *Mass Spectrom. Rev.* **1988,** *7,* 263–358.
3. Thompson, J. J. *Philos. Mag.* **1910,** *18,* 824.
4. Busch, K. L.; Glish, G. L.; McLuckey, S. A. *Mass Spectrometry/ Mass Spectrometry*; VCH: New York, 1988.
5. Jennings, K. R. *Int. J. Mass Spectrom. Ion Phys.* **1968,** *1,* 227–235.
6. Iden, C. R.; Liardon, R.; Koski, W. S. *J. Chem. Phys.* **1972,** *56,* 851.
7. Yu, T.-Y.; Cheng, T. M. H.; Kempter, V.; Lampe, F. W. *J. Phys. Chem.* **1972,** *76,* 3321–3300.
8. (a) Yost, R. A.; Enke, C. G. *J. Am. Chem. Soc.* **1978,** *100,* 2274–2275; (b) Yost, R. A.; Enke, C. G.; McGilvery, D. C.; Smith, D.; Morrison, J. D. *Int. J. Mass Spectrom. Ion Phys.* **1979,** *30,* 127–136.
9. Vestal, M. L.; Futrell, J. H. *Chem. Phys. Lett.* **1974,** *28,* 559–561.

10. Von Zahn, U.; Tatarczyk, H. *Phys. Lett.* **1964,** *12,* 190–191.
11. Gerlich, D. *Adv. Chem. Phys.* **1992,** *82,* 1–176.
12. (a) Gerlich, D. Diplom Thesis, University of Freiburg, 1971; (b) Teloy, E.; Gerlich, D. *Chem. Phys.* **1974,** *4,* 417–427.
13. Squires, R. R.; Lane, K. R.; Lee, R. E.; Wright, L. G.; Wood, K. V.; Cooks, R. G. *Int. J. Mass Spectrom. Ion Processes* **1985,** *64,* 185–191.
14. Marinelli, P. J.; Paulino, J. A.; Sunderlin, L. S.; Wenthold, P. G.; Poutsma, J. C.; Squires, R. R. *Int. J. Mass Spectrom. Ion Processes* **1994,** *130,* 89–105.
15. Schultz, R. H.; Armentrout, P. B. *Int. J. Mass Spectrom. Ion Processes* **1991,** *107,* 29.
16. Ervin, K. M.; Loh, S. K.; Aristov, N.; Armentrout, P. B. *J. Phys. Chem.* **1983,** *87,* 3593. Ervin, K. M.; Armentrout, P. B. *J. Chem. Phys.* **1985,** *83,* 166–189.
17. (a) Hanley, L.; Ruatta, S. A.; Anderson, S. A. *J. Chem. Phys.* **1987,** *87,* 260–268. Blades, A. T.; Klassen, J. S.; Kebarle, P. *Int. J. Mass Spectrom. Ion Processes* **1995,** *141,* 217; (b) Grushow, A.; Ervin, K. M. *J. Am. Chem. Soc.* **1995,** *117,* 11612–11613.
18. Tebbe, K.-F. "Polyhalogen Cations and Polyhalide Anions," in *Homoatomic Rings, Chains and Macromolecules of Main Group Elements;* Rheingold, A. L., Ed.; Elsevier: Amsterdam, 1977.
19. Robbiani, R.; Franklin, J. L. *J. Am. Chem. Soc.* **1979,** *101,* 3709–3715.
20. Ashkenazi, G.; Kosloff, R.; Ruhman, S.; Tal-Ezer, H. *J. Chem. Phys.* **1995,** *103,* 10005–10014, and references therein.
21. Teitelbaum, R. C.; Ruby, S. L.; Marks, T. J. *J. Am. Chem. Soc.* **1980,** *102,* 3322–3328.
22. Wang, T. X.; Kelley, M. D.; Cooper, J. N.; Beckwith, R. C.; Margerum, D. W. *Inorg. Chem.* **1994,** *33,* 5872–5878.
23. Harada, I.; Furukawa, Y.; Tasami, M.; Shirakawa, H.; Ikeda, S. *J. Chem. Phys.* **1980,** *76,* 4746–4757.
24. Hogness, T. R.; Harkness, R. W. *Phys. Rev.* **1928,** *32,* 784–790.
25. Huber, K. P.; Herzberg, G. *Constants of Diatomic Molecules;* Van Nostrand Reinhold: New York, 1979.
26. Kapustinskii, A. F. *Quart. Rev. Chem. Soc.* **1956,** *10,* 283.
27. Topol, L. E. *Inorg. Chem.* **1971,** *10,* 736–740.
28. Finch, A.; Gates, P. N.; Peake, S. J. *J. Inorg. Nucl. Chem.* **1977,** *39,* 2135–2138.
29. Danovich, D.; Hrušák, J.; Shaik, S. *Chem. Phys. Lett.* **1995,** *233,* 249–256.
30. Sharp, S. B.; Gellene, G. I. *J. Phys. Chem.* **1997,** *101,* 2192–2197.
31. Lin, Z.; Hall, M. B. *Polyhedron* **1993,** *12,* 1499–1504.
32. Upschulte, B. L.; Shul, R. J.; Passarella, R.; Keesee, R. G.; Castleman, A. W. *Int. J. Mass Spectrom. Ion Processes* **1987,** *75,* 27.
33. (a) Rebick, C.; Levine, R. D. *J. Chem. Phys.* **1973,** *58,* 3942; (b) Chesnavich, W. J.; Bowers, M. T. *J. Phys. Chem.* **1979,** *83,* 900; (c) Armentrout, P. B. in *Advances in Gas Phase Ion Chemistry, Vol. 1,* Adams, N. G.; Babcock, L. M., Eds.; JAI: Greenwich, 1992.
34. (a) Loh, S. K.; Hales, D. A.; Lian, L.; Armentrout, P. B. *J. Chem. Phys.* **1989,** *90,* 5466; (b) Schultz, R. H.; Crellin, K. C.; Armentrout, P. B. *J. Am. Chem. Soc.* **1991,** *113,* 8590.
35. Lias, S. G.; Bartmess, J. E.; Liebman, J. F.; Holmes, J. L.; Levin, R. D.; Mallard, W. G. *J. Phys. Chem. Ref. Data* **1988,** Suppl. 1. The computerized version used in this work is NIST Standard Reference Database 19, 1993.
36. Lifshitz, C.; Long, F. A. *J. Chem. Phys.* **1964,** *41,* 2468–2471.
37. Palmer, D. A.; Ramette, R. W.; Mesmer, R. E. *J. Sol. Chem.* **1984,** *13,* 673–683.
38. Downs, A. J.; Adams, C. J. in *Comprehensive Inorganic Chemistry,* Bailar, J. C.; Emeleus, J. C.; Nyholm, R.; Trotman-Dickenson, A. F., Eds.; Pergamon: Oxford, 1973.
39. Marcus, Y. *J. Chem. Soc. Faraday Trans. 1* **1987,** *83,* 339–349.
40. Woods, T. L.; Garrels, R. M. *Thermodynamic Values at Low Temperature for Natural Inorganic Materials;* Oxford University Press: Oxford, 1987.
41. Latimer, W. M.; Pitzer, K. S.; Slansky, C. M. *J. Chem. Phys.* **1939,** *7,* 108.
42. Kang, S. H.; Kunc, J. A. *Phys. Rev. A* **1991,** *44,* 3596–3605.
43. Ikezoe, Y.; Matsuoka, S.; Takebe, M.; Viggiano, A. *Gas Phase Ion Molecule Reaction Rate Constants Through 1986,* Maruzen: Tokyo, 1987.
44. Sunderlin, L. S.; Squires, R. R. *Chem. Phys. Lett.* **1993,** *212,* 307–311.
45. Keesee, R. G.; Castleman, A. W. *J. Phys. Chem. Ref. Data* **1986,** *15,* 1011–1071.